JOURNAL OF GEOPHYSICAL RESEARCH, VOL. 106, NO. D16, PAGES 18,205–18,217, AUGUST 27, 2001

Climatology of dust aerosol size distribution and optical properties derived from remotely sensed data in the solar spectrum

D. Tanré,[1] Y. J. Kaufman,[2] B. N. Holben,[3] B. Chatenet,[4] A. Karnieli,[5]
F. Lavenu,[6] L. Blarel,[1] O. Dubovik,[7] L. A. Remer,[2] and A. Smirnov[7]

Abstract. Simultaneous spectral remote observations of dust properties from space and from the ground create a powerful tool for the determination of ambient dust properties integrated on the entire atmospheric column. The two measurement methods have a complementary sensitivity to variety of dust properties. The methodology is demonstrated using spectral measurements (0.47–2.21 μm) from Landsat TM over the bright Senegalian coast and dark ocean, and Aerosol Robotic Network (AERONET) radiances measured in several locations. We derive (1) the dust size distribution, showing a dominant coarse mode at 1–5 μm and a secondary mode around 0.5 μm effective radius; (2) dust absorption, which is found to be substantially smaller than reported from previous measurements; (3) the real part of the refractive index which varies within the range 1.53–1.46; and we show that (4) the effect of the dust nonspherical shape on its optical properties is not significant for scattering angles $<120°$.

1. Introduction

Dust is one of the major components of the aerosol loading observed from space [*Husar et al*., 1997; *Herman et al*., 1997]. Dust is found over Pacific Ocean [*Shaw*, 1980; *Duce et al*., 1980; *Braaten and Cahill*, 1986; *Prospero et al*., 1989; *Nakajima et al*., 1989], over the Mediterranean Sea [*Chester et al*., 1984; *Reiff et al*., 1986; *Bergametti et al*., 1989; *Dulac et al*., 1992], with the highest concentrations found over the equatorial and tropical North Atlantic. Saharan dust is the main source of mineral dust over the globe [*Carlson*, 1979; *Schütz*, 1979; *Glaccum and Prospero*, 1980; *Prospero*, 1981; *Talbot et al*., 1986; *Li et al*., 1996].

These Saharan air outbreaks observed during the past decades [e.g., *Prospero*, 1981; *Morales*, 1986; *Pye*, 1987] are covering very large areas with large dust concentrations, so they were suspected to have a significant radiative impact on climate and on remote sensing of the ocean productivity. Several authors computed the dust radiative forcing [*Carlson and Benjamin*, 1980; *Joseph*, 1984; *Tanré et al*., 1984; *Ackerman and Chung*, 1992; *Sokolik and Toon*, 1996; *Tegen et al*., 1996] with dust optical characterization derived from in situ measurements [*Jaenicke and Schütz*, 1978; *d'Almeida et al*., 1991; *Wendish and Von Hoyningen-Huene*, 1994; *Sokolik et al*., 1998]. Although all these studies show that the dust impact on climate is expected to be important, its magnitude still remains uncertain since the use of in situ measurements suffers from measurement uncertainties [*Heintzenberg et al*., 1997] and cannot be representative of the entire vertical atmospheric column.

In this paper we propose to derive the Saharan dust properties using a combination of data remotely sensed from space and the ground. The advantage of the use of remote sensing techniques is that they measure the properties of the ambient dust, not affected by processing by the in situ instruments, and thus the parameters are of direct relevance to radiative forcing of climate. The surface observations are acquired by the Sun photometers of the Aerosol Robotic Network (AERONET) program [*Holben et al*., 1998a], and the satellite images were acquired by the Thematic Mapper (TM) during a field experiment in Senegal in 1987 [*Tanré et al*., 1988a]. Satellite and ground-based remote sensing supplement each other in their methods of dust observations. The surface-based measurements are of sunlight scattered by the dust at scattering angles of 3°–120°, measured against the black deep space; the satellite measurements are in the backscattering direction (scattering angle of 148° in the present case) and are collected over dark ocean and nearby bright desert. Therefore the size distribution is derived from the surface sky radiances, while the spectral refractive index and the single-scattering albedo are derived both from the satellite images [*Kaufman*, 1987] and from the surface sky radiances [*Dubovik et al*., 1998]. The impact of possible nonsphericity effects is discussed, and a comparison with previous studies is provided.

2. Method

The remote sensing method is based on the use of several remote sensing data sets, each with different sensitivity to the dust properties in order to derive all the relevant optical parameters: (1) the dust size distribution is derived from the

[1]Laboratoire d'Optique Atmosphérique, CNRS Université des Sciences et Technologies de Lille, Villeneuve d'Ascq, France.
[2]NASA Goddard Space Flight Center, Laboratory for Atmospheres, Greenbelt, Maryland.
[3]NASA Goddard Space Flight Center, Laboratory for Terrestrial Physics, Greenbelt, Maryland.
[4]Laboratoire Interuniversitaire des Systèmes Atmosphériques, Universités Paris VII et Paris XII, Créteil, France.
[5]Institute for Desert Research, Ben Gurion University, Sede-Boker, Israel.
[6]CESBIO Centre National d'Etudes Spatiales, Toulouse, France.
[7]Science Systems and Applications Inc., Laboratory for Terrestrial Physics, NASA GSFC, Greenbelt, Maryland.

Paper number 2000JD900663.
0148-0227/01/2000JD900663$09.00

Table 1. Location of the AERONET Stations Selected for the Present Study (single asterisk, April, May and June are missing; double asterisks, December is missing; triple asterisks, March, April, May, and September are missing)

Name	Country	Latitude	Longitude	Acquisition Period
Sal Island	Cape Verde	N 16°43′	W 22°56′	Oct. 1994/June 1995 Oct. 1995/July 1996 Jan. 1997/Nov. 1997*
Sede Boker	Israel	N 30°31′	E 34°28′	March 1995/Sept. 1996** Sept. 1997/Dec. 1998
Banizoumbou	Niger	N 13°32′	E 02°39′	Jan. 1996/Dec. 1996 Jan. 1997/Oct. 1997***

AERONET sky aureole; (2) Landsat TM data over the land, using a balance between dust scattering and absorption of light reflected by the bright surface, are used to derive the dust spectral single-scattering albedo (related to the spectral imaginary index of refraction); (3) Landsat TM data over the ocean at 148° scattering angle serve as a closure to the dust properties and bound the real part of the refractive index; (4) AERONET sky radiances, at scattering angle of 120° and 90°, add information on the dust nonsphericity effect on the scattering phase function; (5) AERONET sky radiances over the whole almucantar are used to confirm the values of the single-scattering albedo. The uncertainties in the size distribution and refractive index values retrieved from AERONET data are discussed by *Dubovik et al*. [2000]. The analysis of the satellite data is described by *Kaufman* [1987].

The dust size distribution is derived from the aureole sky radiance for scattering angles less than 40° from the Sun [*Nakajima et al*., 1996]. In this scattering range the results are not very sensitive to the particle refractive index [*Santer and Herman*, 1983; *Kaufman et al*., 1994; *Nakajima et al*., 1996] and to the particle shape [*Mishchenko et al*., 1997]. The inversion scheme uses the sky radiances in the four spectral bands 0.440, 0.670, 0.870, and 1.020 μm for scattering angles between 3° and 40°. The accuracy has been shown to be within 4–10% in the radius range of 0.10–6.0 μm [*Kaufman et al*., 1994], but near both bounds of the inversion interval (0.05 and 8 μm), the inverted particle concentration is artificially larger to account for the assumed zero concentrations outside of these bounds [*Remer and Kaufman*, 1998]. In a similar way, systematic errors due to instrumental problems may lead to a larger inaccuracy [*Dubovik et al*., 2000], but the data set used in the present study results from several different instruments, with partially random errors, a fact that should reduce the average error. The single-scattering albedo is derived from the AERONET data using the method developed by *Dubovik et al*. [1998, 2000]. The shape of the aerosol particles can affect the measured radiances for large scattering angles [*Mishchenko et al*., 1997; *Dubovik et al*., 2000]. Therefore comparisons of computations based on Mie theory with AERONET measurements allow to asses the validity of the spherical model.

Space-borne measurements over bright land have the strongest sensitivity to dust absorption [*Fraser and Kaufman*, 1985]; the sunlight, reflected by the surface, travels twice through the dust layer, on its way down and up, doubling the absorption probability for the reflected photons. To derive the dust absorption, we assume that the particles have a homogenous composition. Therefore the absorption by dust can be represented by the imaginary index. This analysis of the dust absorption is similar to the procedure used earlier [*Kaufman*, 1987; *Kaufman et al*., 1990; *Ferrare et al*., 1990] but with a better characterization of the dust particle size. The method requires a couple of images with a different aerosol loading but close enough in time, view, and illumination directions to assume that the surface properties did not change between the two acquisitions. The real part of the refractive index is evaluated from the satellite data over the ocean. These data are less sensitive to absorption than the data over the land due to the very low surface reflectance and as a result more sensitive to aerosol scattering properties and refractive index.

3. Database

We use the Sun/sky observations acquired at several locations in and around the African continent by the instruments of the AERONET program [*Holben et al*., 1998a]. The satellite approach is applied to Landsat/Thematic Mapper data collected over Senegal with simultaneous measurements from the ground of the dust optical thickness [*Tanré et al*., 1988a, 1988b].

3.1. Sun/Sky Radiances

The AERONET network is a global network of Sun/sky autonomous radiometers. Description of the instruments and data acquisition procedure is given by *Holben et al*. [1998a]. Measurements from three stations around the Saharan desert are used. The exact locations are given in Table 1. We selected Sal Island (Cap Verde) on the West, Sede Boker (Israel) on the East, for getting the dust properties as it emerges from the two sides of the Sahara. Banizoumbou (Niger), located on the southern edge of the desert, is the station that is more representative of dust properties near the sources. These stations operated at least for several months and the time period is also reported in Table 1.

Sky and Sun measurements are performed in four spectral bands, 0.44, 0.67, 0.87, and 1.02 μm, from which the aerosol content, the size distributions, and the single-scattering albedo are derived. Calibration coefficients for the optical thickness measurements are based on an intercomparison with a reference instrument that was calibrated using Langley plots from data collected at the pristine Mauna Loa location. Radiance measurements are calibrated using the 2 m integrating sphere at NASA Goddard Space Flight Center [*Holben et al*., 1998a]. The total uncertainty $\Delta\tau$ in the optical thickness is around 0.01. The uncertainty in the sky radiance measurements is assumed to be $<\pm 5\%$ for all channels at the time of calibration. Since the calibration may deteriorate as a function of time, instruments are calibrated every 8–10 months and data are corrected for possible trend. Data sets used in this study were fully calibrated and verified.

3.2. Satellite Data

The Landsat TM data were collected 80 km south of Dakar, Senegal, simultaneously with Sun photometer measurements from the ground [*Tanré et al*., 1988a] in May and April 1987. The TM sensor has six spectral bands between 0.49 μm and 2.1 μm which allows us to characterize the aerosol properties over the whole solar spectrum. The images include both land and ocean. Since the data are for a scattering angle of 148°, we do not expect significant effects of particle nonsphericity [*Mishchenko et al*., 1997], but this assumption will be discussed in section 4.5. We assume that the dust particle size derived from Cap Verde Station is also representative of the measurements over the Senegalian coast.

Data from May 3, 1987, are used as the less dusty-"clear" day; the optical thickness at 0.64 μm is equal to 0.8 [*Tanré et al*., 1988a]. The TM apparent reflectance allows to derive the surface reflectance ρ after the atmospheric correction is performed, using the ground-based measured optical thickness [*Tanré et al*., 1988b]. Then, the surface reflectance ρ is used to calculate the expected apparent reflectance in the dusty day, April 15 1987, using again the ground-based measured optical thickness (optical thickness at 0.64 μm of 2.4). The aerosol properties, i.e., the single-scattering albedo over land and the real part of the refractive index over the ocean, are adjusted to get the best match between the theoretical computations and the TM data.

4. Results

4.1. General Evolution of the Optical Thickness and Angström Exponent

Climatology of the occurrence of dust is represented by histograms of the aerosol optical thickness τ measured at 0.670 μm by the Sun-sky radiometers and by the Angström exponent α derived from τ measured at 0.870 and 0.440 μm for the three sites,

$$\alpha = \ln(\tau_{865}/\tau_{440})/\ln(0.865/0.440). \quad (1)$$

Although the time periods are not identical for the three sites, they cover long enough periods to represent the dust "climatology" in these sites. Figure 1 shows the cumulative probability distribution of τ and α. As expected, the station closest to the sources, i.e., the Banizoumbou site, shows the largest optical thickness (median value of $\tau_{670} = 0.44$) associated with the smallest Angström exponent (median value of $\alpha = -0.07$) due to the presence of very large dust particles. The probability distribution for Sal Island is shifted to lower values of τ (median value of $\tau_{670} = 0.31$) with smaller particles (median value of $\alpha = -0.23$). The results confirm the predominance of mineral dust over the Cape Verde Islands due to the western trade winds. The aerosol regime in Sede Boker is clearly different. Particles are smaller ($\alpha = -0.56$), and the aerosol loading is low when compared to the other sites ($\tau_{670} = 0.17$). Nevertheless, the site is affected by the presence of dust particles since values of α are less negative (-0.3 to -1.0 for the central 50%) than what would be expected for an urban/industrial aerosol model [*Remer et al*., 1999]. Presence of maritime aerosols could also explain these α. A complete description of the seasonal evolution as well as the variations observed over several years is given by *Holben et al*. [1998b].

4.2. Size Distribution From Surface-Based Measurements

To invert the aureole part of the sky and derive the aerosol size distribution, the aerosol concentration and properties should be homogeneous in the aureole region. Such conditions may not be met for high aerosol optical thicknesses. Therefore inversions were performed only for optical thickness smaller than 0.8, which represents 80, 90, and 95% of the total observations in Banizoumbou, Sal Island, and Sede Boker, respectively (see Figure 1). The size distributions (Figure 2) are sorted according to increasing aerosol optical thickness at 1.020 μm. The approach was used to characterize the urban/industrial aerosols [*Remer and Kaufman*, 1998] and the biomass burning aerosols [*Remer et al*., 1998] and is extended hereinafter to dust aerosols.

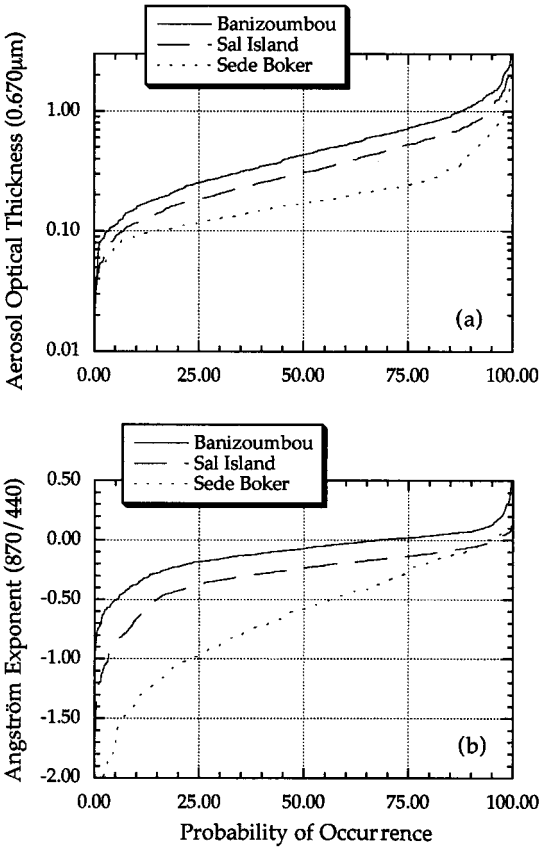

Figure 1. (a) Histograms, for the three selected sites, of optical thickness at 670 nm and (b) Angström exponents derived from the optical thickness measurements at 440 and 870 nm.

Results of the inversion to data acquired in the three stations are reported in Figures 2a, 2b, and 2c for Banizoumbou, Sal Island, Sede Boker, respectively. The optical thickness values used to sort the size distributions have been selected to be similar in the three sites except that in Sede Boker. In Sede Boker there were not enough measurements with high aerosol optical thickness, therefore the maximum optical thickness is half of the value for the two other sites.

For very clean conditions ($\tau \leq 0.04$), both Sal Island and Sede Boker sites show a similar size distribution with three modes, one accumulation mode with radius r, $r < 0.3$ μm, and two modes of larger particles with radii near 1.5 and 2.5 μm. These two coarse modes may be attributed to the presence of salt due to marine influence [*Chiapello et al*., 1999] or due to the presence of dust. Marine aerosols of similar size were detected on the east coast of the United States [*Remer et al*., 1999]. For the same low-turbidity conditions at the Banizoumbou site, there is still a mode at around 1.5 μm, but the mode at 2.5 μm is less well defined. The biggest differences are

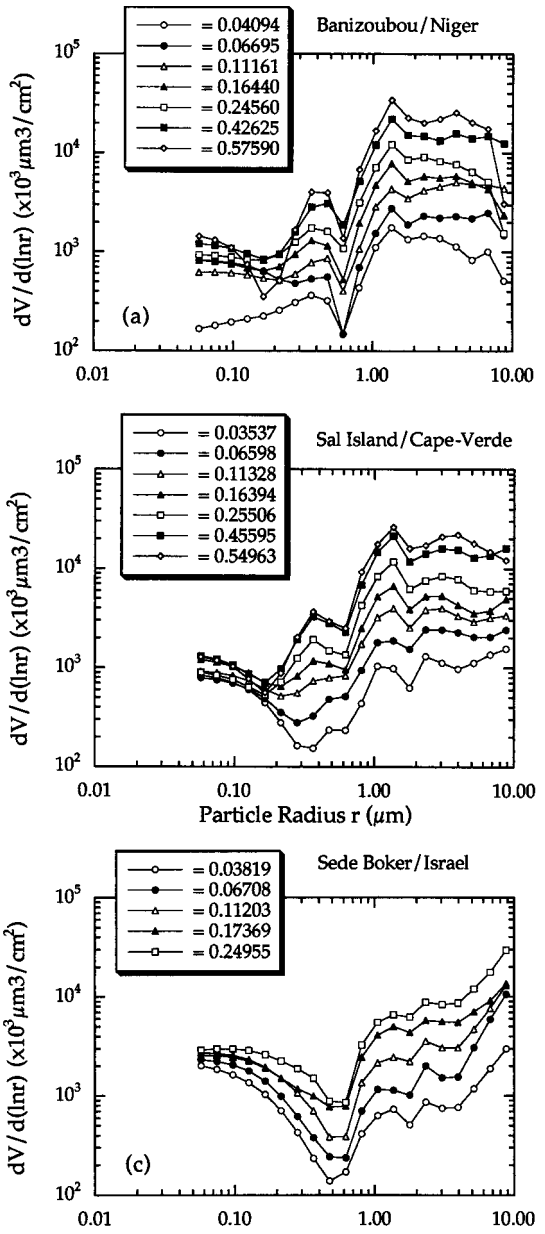

Figure 2. Volume size distribution derived from the sky radiances as a function of the particle radius. The distributions have been averaged over 10–15 individual size distributions and sorted according to the aerosol optical thickness measured at 1020 nm. (a) Banizoumbou, (b) Sal Island, (c) Sede Boker.

observed in Banizoumbou with the appearance of mode of particles with radii near 0.4–0.5 μm coincident with disappearance of the accumulation mode (Figure 2a). The appearance of this mode can be attributed to clay particles and is representative of the Saharan dust influence.

For larger optical thickness ($\tau \sim 0.25$) the Sal Island site (Figure 2b) shows a behavior similar to the Banizoumbou site with the appearance of a mode around 0.3–0.4 μm. This mode is not present in Sede Boker where the curves for the range of τ values are very similar except of a higher volume (Figure 2c). For large values of τ (around ~0.60) the 0.3–0.4 μm mode is well defined for Banizoumbou with a steep decrease around radius of 0.6 μm; the curves are smoother in Sal Island.

Several parameters that describe the aerosol size distribution can be derived from it. For large particles the effective radius defined by

$$r_{\text{eff}} = \int_0^\infty r^3 n(r)\, dr \Big/ \int_0^\infty r^2 n(r)\, dr \qquad (2)$$

is quite representative of the optical properties. For small particles a more appropriate parameter is the volume-weighted radius r_v defined by

$$r_v = \int_0^{r_{\max}} r\{dV/dr\}\, dr \Big/ \int_0^{r_{\max}} \{dV/dr\}\, dr \qquad (3)$$

which implicitly considers that the extinction efficiency varies linearly with the size of small particles. The plots in Figure 2 show that the upper limit $r_{\max}$ should be 0.6 μm to separate the accumulation mode from the coarse mode in the computation of r_v.

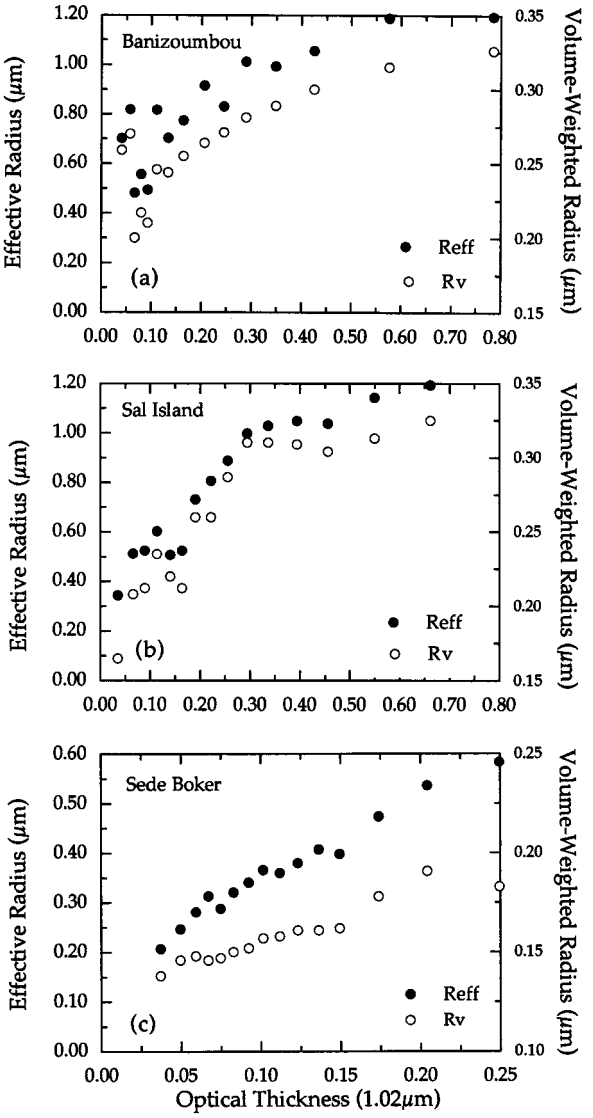

Figure 3. Effective radius r_{eff} of the total size distribution and volume-weighted radius r_v of the accumulation mode for the three sites as a function of the optical thickness measured at 1.02 μm. The upper limit $r_{\max}$ (equation (3)) is chosen to be 0.6 μm for separating the accumulation mode from the coarse mode.

Table 2. (1) Linear Regression Equation and Correlation Coefficient Relating the Effective Radius of the Total Size Distribution to the Optical Thickness at 1.02 μm; (2) As for (1) But for the Volume-Weighted Radius of the Accumulation Mode ($r < 0.6$ μm); Column 4 Corresponds to the Effective Radius of the Coarse Mode Only ($r > 0.6$ μm)

Name	Equations	Correlation Coefficient	R_{eff} (Coarse), μm
Banizoumbou	(1) R_{eff} (μm) = 0.62 + 0.91 × τ(1.02 μm)	0.86	2.19 ± 0.12
	(2) R_v (μm) = 0.23 + 0.14 × τ(1.02 μm)	0.84	
Sal Island	(1) R_{eff} (μm) = 0.42 + 1.39 × τ(1.02 μm)	0.93	2.15 ± 0.10
	(2) R_v (μm) = 0.20 + 0.24 × τ(1.02 μm)	0.88	
Sede Boker	(1) R_{eff} (μm) = 0.17 + 1.70 × τ(1.02 μm)	0.99	3.01 ± 0.24
	(2) R_v (μm) = 0.13 + 0.24 × τ(1.02 μm)	0.96	

Figure 3 shows r_v and r_{eff} as a function of the optical thickness measured at 1.02 μm for the three sites. Note that the effective radius is computed here for the total size distribution. All sites show an increase of both radii as the aerosol content increases. Banizoumbou and Sal Island display a smaller slope when the optical thickness reaches a value around 0.5. A linear regression gives high-correlation coefficients (Table 2). For the Sede Boker site, the corresponding values are in a very good agreement (when scaled from the present wavelength 1.02–0.67 μm) with the values obtained by *Remer and Kaufman* [1998] for pollution over the eastern part of the United States. In Table 2 the effective radius of the coarse mode only is also reported. It is quite stable and independent of the aerosol content. Let us note that the results for Sede Boker are less reliable at the upper limit of the retrieval, and the corresponding results may not be representative.

4.3. Real Refractive Index From Satellite Over the Ocean

At this stage both real and imaginary parts of the refractive index are undetermined. To derive the real part of the refractive index, we use the TM data over dark ocean since they are not very sensitive to dust absorption (which will be determined in the next session). When the single-scattering albedo changes from 0.96 to 0.87, the reflectance at 670 nm for $\tau = 0.8$ changes by more than 40% over land and by 10% only over ocean.

The results are summarized in Figure 4 where both the spectral Landsat data and the calculated values are plotted. The *Ahmad and Fraser* [1982] radiative code is used in the computations. Two values of the effective radius are considered in Figure 4a, 1.5 and 2.5 μm, which is the expected range of the radii for the April 17, 1987, dust event. The computations have been performed for values of the real part of the refractive index found in the literature [*WMO*, 1983], $n_r = 1.53$ for $\lambda = 0.47$ μm to $\lambda = 0.86$ μm, $n_r = 1.40$ for $\lambda = 1.65$ μm, and $n_r = 1.22$ for $\lambda = 2.10$ μm [see *Jursa*, 1985] when the imaginary part is taken from the analysis performed in section 4.4. In Figure 4b, for an effective radius of 1.5 μm, a second set of the real part of the refractive index n_r is considered with a constant value equal to 1.46.

The measured apparent reflectance is located between the two effective radii used in the calculations (Figure 4a). The very low refractive index of 1.22 at 2.1 μm is not consistent with the Landsat value at this wavelength (Figure 4a). The index of 1.46 for 1.65 and 2.1 μm fits the data better (Figure 4b). A higher index would result in radiances that are higher than the measured radiances at 1.65 μm and at 2.1 μm in the clear day. For the short wavelengths, there is no sensitivity to the difference between refractive index of 1.53 and 1.46 due to the large ratio between the effective particle size and the wavelength.

To summarize, a good consistency is obtained for a real refractive index around 1.53 for all wavelengths up to 0.86 μm and around 1.46 at 1.65 and 2.10 μm. The results are based on a single case, but it is very difficult to duplicate the present

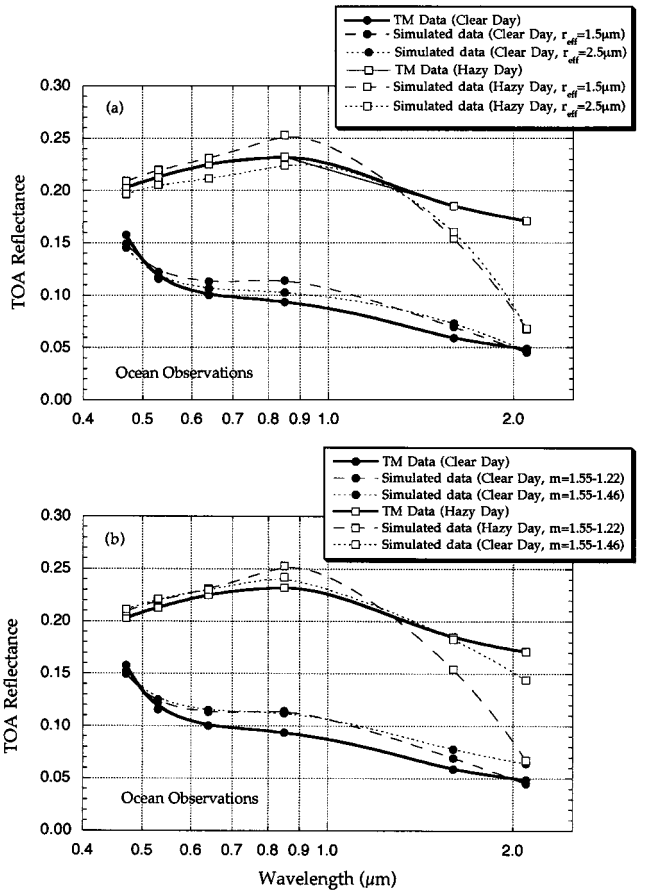

Figure 4. Apparent reflectance as a function of the wavelength measured by Landsat TM over the ocean for the "clear" (less dusty) day ($\tau = 0.8$) and the dusty day ($\tau = 2.4$). Theoretical computations are shown for the imaginary index derived in section 4.4. (a) Two values of the effective radius are considered, 1.5 and 2.5 μm, when the real part of the refractive index is varying ($n_r = 1.53$ for $\lambda = 0.47$ μm to $\lambda = 0.86$ μm, $n_r = 1.40$ for $\lambda = 1.65$ μm and $n_r = 1.22$ for $\lambda = 2.1$ μm). (b) Two sets of the real part of the refractive index are considered same as in Figure 4a (i.e., $n_r = 1.53$ for $\lambda = 0.47$ μm to $\lambda = 0.86$ μm, $n_r = 1.40$ for $\lambda = 1.65$ μm and $n_r = 1.22$ for $\lambda = 2.1$ μm) and a fixed value ($n_r = 1.46$); the effective radius is taken equal to 1.5 μm.

study because TM data are not routinely acquired over Africa. Our results will be confirmed soon by the use of the MODIS data since the instrument has a global daily coverage and has the same spectral capability that the TM sensor.

4.4. Spectral Imaginary Index and Single-Scattering Albedo From Satellite and Surface-Based Measurements

The single-scattering albedo can be derived from space [*Fraser and Kaufman*, 1985]. For brighter surfaces (reflectance of 0.25) the effect of ω_0 is much stronger than over dark surfaces, like the ocean used in section 4.3. It determines if the dust will increase (high ω_0) or decrease (low ω_0) the apparent reflectance. This balance depends on the particle effective size and refractive index. The sensitivity of the apparent reflectance to ω_0 is even higher for brighter desert surfaces. Over a bright surface, dust can absorb the direct solar radiation and radiation reflected from the Earth surface, increasing the absorption efficiency. Whether the balance between dust scattering and absorption is positive or negative for a given surface reflectance, depends on the size of dust particles and their optical properties. A sensitivity study performed by *Kaufman* [1987] showed that the principal sources of uncertainty come from possible variation of the aerosol scattering properties, variation in the surface reflectance or in the calibration coefficients between the two dates. Both images are close enough in time to assume that the two last sources of error have no impact. With the ground measurements that were performed simultaneously to the satellite data acquisition [*Tanré et al*., 1988a], it can be assumed that the aerosol characteristics did not change between the clear and the hazy days. As a result, we can expect an accuracy of ω_0 of $\Delta\omega_0$ around 0.03 [*Kaufman*, 1987].

The method is applied again to the TM images. Data from May 3, 1987, are used as the less dusty-"clear" day (Sun photometer measured optical thickness at 0.64 μm of $\tau_{64} = 0.8$) to derive the desert reflectance ρ. Then ρ is used to calculate the expected apparent reflectance ρ_c^* in the dusty day, April 17, 1987, for the optical thickness measured by the Sun photometer ($\tau_{64} = 2.4$). The derived dust single-scattering albedo is the value of ω_0 for which the calculated apparent reflectance ρ_c^* fits the measured value in the dusty day ρ_m^*. The analysis is repeated for all the Landsat spectral channels to derive the spectral single-scattering albedo.

To explain over the high surface reflectance of ~0.3, the increase in the Earth-surface reflectance of 0.06 (Figure 5) due to the presence of dust, a close to zero absorption ($\omega_0 \sim 1$) has to be used. Even an imaginary index of $n_i = -0.004$ ($\omega_0 = 0.83$ at $\lambda = 0.65$ μm), half of the WMO value, would cause a decrease rather than increase in the apparent reflectance. Uncertainty in the effective radius or real part of the refractive index result in uncertainty of only $\Delta n_i = \pm 0.0005$ in the imaginary index or $\Delta\omega_0 = \pm 0.005$. A significant imaginary part of the refractive index was found for the TM-0.47 μm channel: $n_i = -0.003 \pm 0.0003$ and for the 1.65 μm channel, $n_i = -0.001 \pm 0.0005$. For the rest of the wavelengths the value is close to zero within the uncertainty of ± 0.0003 in the derivation. The corresponding single-scattering albedo is around 0.88 in the blue and larger than 0.98 for $\lambda > 0.6$ μm (Y. J. Kaufman, Absorption of sunlight by dust as inferred from satellite and ground-based remote sensing, submitted to *Geophysical Research Letters*, 2000) (hereinafter referred to as K2000).

The method developed by *Dubovik et al*. [2000] for deriving the single-scattering albedo ω_0 from ground-based measurements has been also applied to the AERONET data. Since the accuracy of the inversion is decreasing for low-aerosol optical thickness, only data corresponding to an optical thickness larger than 0.3 at 1.02 μm have been inverted, which means that there is no ω_0 derivation for the Sede Boker site. Mean value ϖ_0 and standard deviation σ of the spectral single-scattering albedo derived from the AERONET measurements

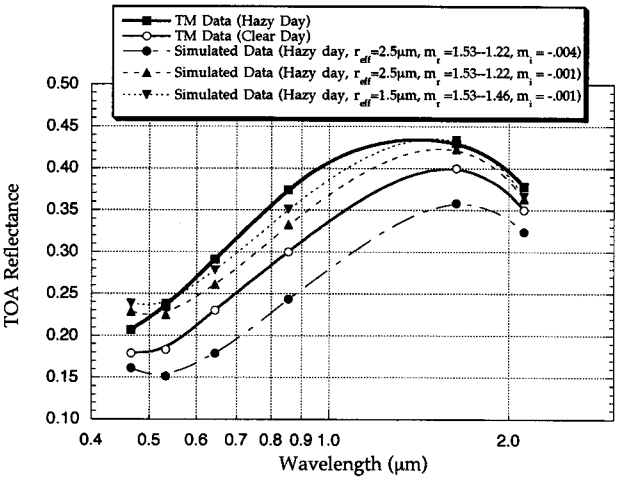

Figure 5. Apparent reflectance at the top of the atmosphere over the land in Senegal measured by Landsat TM (solid lines) for optical thickness τ of 0.8 (open circles) and 2.4 (squares). The measurements are compared with several calculations (thin lines). The dashed-dotted line corresponds to an effective radius of 2.5 μm with an imaginary refractive index, n_i, equal to -0.004 when the real part of the refractive index is varying ($n_r = 1.53$ for $\lambda = 0.47$ μm to $\lambda = 0.86$ μm, $n_r = 1.40$ for $\lambda = 1.65$ μm and $n_r = 1.22$ for $\lambda = 2.1$ μm). The dashed lines correspond to the same aerosol model, but the imaginary refractive index n_i is equal to -0.001. The dotted line corresponds to an effective radius of 1.5 μm with an imaginary refractive index n_i equal to -0.001 when the real part of the refractive index is taken from the analysis performed in section 4.3 (i.e., $n_r = 1.53$ for $\lambda = 0.47$ μm to $\lambda = 0.86$ μm, $n_r = 1.46$ for $\lambda = 1.65$ μm and $\lambda = 2.1$ μm).

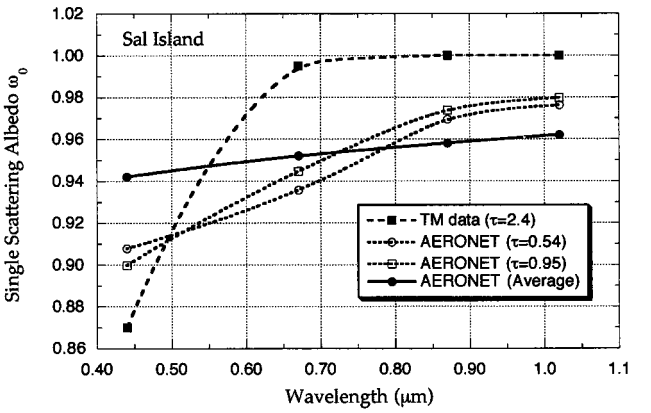

Figure 6. Single-scattering albedo of the dust as a function of the wavelength in different conditions. The dashed line corresponds to the TM image near the African coast with a high aerosol content ($\tau = 2.4$ at 0.55 μm). The dotted lines correspond to AERONET data acquired in July 1999 over the Sal Island for two turbidity conditions ($\tau = 0.54$ and 0.95 at 0.55 μm). The solid line corresponds to the average over the time period.

Table 3. Mean Value ϖ_0 and Standard Deviation σ of the Spectral Single-Scattering Albedo Derived From the AERONET Measurements Performed at the Sal Island and the Banizoumbou Sites

Name	$\lambda = 0.441$ μm	$\lambda = 0.670$ μm	$\lambda = 0.870$ μm	$\lambda = 1.020$ μm
Sal Island	$\varpi_0 = 0.94$	$\varpi_0 = 0.95$	$\varpi_0 = 0.96$	$\varpi_0 = 0.96$
	$\sigma = 0.05$	$\sigma = 0.04$	$\sigma = 0.04$	$\sigma = 0.04$
Banizoumbou	$\varpi_0 = 0.95$	$\varpi_0 = 0.96$	$\varpi_0 = 0.97$	$\varpi_0 = 0.97$
	$\sigma = 0.03$	$\sigma = 0.03$	$\sigma = 0.02$	$\sigma = 0.02$

The inversion has been performed for τ at 1020 nm larger than 0.3. The main source of error in the derived single-scattering albedo is due to calibration of the sky data. It is estimated to be ±0.03.

performed at the Sal Island and the Banizoumbou sites are reported in Table 3 for the four wavelengths. Values are similar for both sites with smaller ω_0 for Sal Island. The values of ω_0 derived from the AERONET analysis are higher in the blue (0.94 compared to 0.88) and smaller (0.96 compared to 0.98) in the red than the values derived from TM images (Figure 6). There are several possible explanations. First, the TM data correspond to a very high aerosol content ($\tau = 2.4$) which is not included in the AERONET database. It is one of the largest dust events observed in the area, so it is not representative of the mean conditions. In addition, our data set may be affected by the presence of other aerosol types. A careful analysis of individual measurements to ensure the presence of pure dust for two aerosol contents, $\tau = 0.54$ and 0.95 (dotted lines) shows that there is a transition regime between the extreme TM case and the dust background conditions.

The low values of the absorption that we derive differ from the relatively high values previously obtained from in situ measurements; for example, we do not find the very low values (0.6–0.7) reported in the literature [*Jursa*, 1985; *WMO*, 1983]. As pointed out by K2000, remote sensing techniques are expected to be more accurate than in situ measurement since they are not affected by errors resulting from sampling problems reported by *Heintzenberg et al*. [1997] (Figure 6).

4.5. Particle Nonsphericity From Surface-Based Measurements

All the parameters of the dust particles that describe their optical properties, for example, effective radius, single-scattering albedo, and refractive index are now determined. Any significant differences between the calculated phase function and the measurements should be due to particle nonsphericity. To measure the effects of nonsphericity directly, we use the rate of change in sky radiance, measured from the ground, with a change in the dust optical thickness as a surrogate for the scattering phase function.

Let us write formally the equation. The normalized sky radiance $\rho_s(\tau, \theta, \theta_0, \phi)$, where τ is the aerosol optical thickness, θ is the view direction, θ_0 is the solar zenith angle, and ϕ is the azimuth of the scattered radiation from the solar beam, is approximated, in apparent reflectance units, by

$$\rho_s(\tau, \theta, \theta_0, \phi) = \rho_{\text{aerosol}}(\tau, \theta, \theta_0, \phi) + \rho_{\text{Rayleigh}}(\theta, \theta_0, \phi) + f(\tau, \rho'), \quad (4)$$

where ρ_{aerosol} is the aerosol contribution to the sky radiance; ρ_{Rayleigh} is the Rayleigh contribution; $f(\tau, \rho')$ is the contribution of the surface with ρ' the surface average reflectance.

The rate of change in sky radiance with a change in the dust optical thickness, i.e., the slope $\Delta\rho_s(\tau, \theta, \theta_0, \phi)/\Delta\tau$, is therefore given by

$$\Delta\rho_s(\tau, \theta, \theta_0, \phi)/\Delta\tau = \Delta\rho_{\text{aerosol}}(\tau, \theta, \theta_0, \phi)/\Delta\tau + f(\tau, \rho')/\Delta\tau, \quad (5)$$

and in the single-scattering approximation,

$$\Delta\rho_s(\tau, \theta, \theta_0, \phi)/\Delta\tau = \omega_0 P(\theta, \theta_0, \phi)/4\mu_0\mu + K\beta\rho', \quad (6)$$

where ω_0 is the single-scattering albedo, $P(\theta, \theta_0, \phi)$ the scattering phase function, β the backscattering coefficient of the aerosol, and K a constant depending on the geometry conditions.

The impact of nonsphericity on the phase function has been shown to depend on the scattering angle [*Nakajima et al*., 1989; *Mishchenko et al*., 1997; *Von Hoyningen-Huene and Posse*, 1997]. The impact is minimal at scattering angles around 90° and 150° and maximum at 120°. Therefore the slopes $\Delta\rho_s(\tau, \theta, \theta_0, \phi)/\Delta\tau$ should be substantially different for scattering angles of 90° and 120°. Consistent differences from Mie theory for both scattering angles could not be attributed to nonsphericity effects. Therefore the dust scattering in these two scattering angles is examined here. Scattering angle of 120°, corresponds to solar zenith angle of 60°, view angle of 60° and anti-solar direction; scattering angle of 90° is obtained for same zenith angles and an azimuth of 110° from the Sun. Multiple

Table 4a. Correlation Coefficients Between the Radiances and the Optical Thicknesses for the Three Sites, the Four Wavelengths, and Both Geometrical Conditions, $\Theta = 120°$ and 90°

	$\Theta = 120°$				$\Theta = 90°$			
	0.44 μm	0.67 μm	0.87 μm	1.02 μm	0.44 μm	0.67 μm	0.87 μm	1.02 μm
Banizoumbou 1996	78	94	92	92	90	96	95	95
Banizoumbou 1997	55	94	92	93	81	95	95	94
Sal Island 1994–1995	63	98	95	96	10	92	94	95
Sal Island 1996–1997	43	92	91	87	83	94	93	90
Sede Boker 1996–Jan./June	47	94	92	97	63	95	98	98
Sede Boker 1998–May/Oct.	74	98	99	98	84	99	99	99

Table 4b. Intercept That Corresponds to the Linear Regression and Theoretical Computations for Molecular Scattering With Two Surface Types, First for a Rayleigh Atmosphere With a Black Surface, then, for a Rayleigh Atmosphere Over a Reflecting Surface With an Albedo of 0.1, 0.2, 0.4, and 0.4 at 0.44 μm, 0.67 μm, 0.87 μm, and 1.02 μm

	$\Theta = 120°$				$\Theta = 90°$			
	0.44 μm	0.67 μm	0.87 μm	1.02 μm	0.44 μm	0.67 μm	0.87 μm	1.02 μm
Banizoumbou 1996	10.0	2.3	0.7	0.3	08.9	2.0	0.6	0.2
Banizoumbou 1997	10.0	2.0	0.5	0.2	08.9	1.7	0.6	0.4
Sal Island 1994–1995	11.0	2.3	0.8	0.5	11.0	2.3	0.7	0.3
Sal Island 1996–1997	11.0	1.6	0.3	0.0	09.5	1.1	0.1	0.3
Sede Boker 1996–Jan./June	11.0	2.8	1.2	0.7	10.0	2.6	1.1	0.6
Sede Boker 1998–May/Oct.	13.0	2.9	1.0	0.4	12.0	2.7	0.9	0.2
Theoretical computation $\rho_s = 0.0$	10.3	2.1	0.7	0.4	09.1	1.7	0.6	0.3
Theoretical computation $\rho_s = 0.1; 0.2; 0.4; 0.4$	11.1	2.5	1.0	0.5	09.6	2.1	0.9	0.5

scattering will decrease the sensitivity of the slope to the value of the phase function. We restricted our study to a moderate range of optical thickness, e.g., $\tau \leq 0.6$. For each site we distinguished several time periods for detecting possible instrumental problems due to filter degradation or drift in the calibration that would not have been detected during the data processing.

In Table 4a the correlation coefficients between the radiances and the optical thickness is reported for the three sites, the four wavelengths, and both geometrical conditions. The high-correlation coefficients show that the measurements are linearly correlated with the optical thickness in most cases, except in the blue (0.44 μm). The low correlation may indicate the variability of the absorption in this spectral range.

In Table 4b we report the intercept that corresponds to the molecular scattering $\rho_{\text{Rayleigh}}(\theta, \theta_0, \phi)$ in addition to the surface contribution $f(0, \rho')$. The two last rows correspond to theoretical computations, first for a Rayleigh atmosphere with a black surface, then for a Rayleigh atmosphere over a reflecting surface with an albedo of 0.1, 0.2, 0.4, and 0.4 at, respectively, 0.44, 0.67, 0.87, and 1.02 μm. Both simulations give the magnitude of the variability due to the uncertainty in the surface. The intercepts are close to the clean atmospheric values, i.e., Rayleigh scattering, indicating correct calibration, except in Cape Verde in 1996–1997. The corresponding data are excluded hereinafter.

The slopes are reported in Table 4c. As expected from the correlation coefficient in Table 4a, the slopes at 0.44 μm are very variable. The variability is significantly smaller in the longer wavelengths, indicating consistency among the three locations and the period of measurements. It is also consistent with absence of absorption. To compare with Mie theory, the last rows give the slopes in four different conditions; for a black surface with two aerosol models that correspond to values of the effective radius of 1.5 and 2.5 μm, which bounds the range of our retrieved values, and also for the same aerosol models but for a surface albedo of 0.1, 0.2, 0.4, and 0.4 at 0.44, 0.67, 0.87, and 1.02 μm, respectively. There is clearly no strong discrepancies between the measured and the computed values.

A comparison between the measured slopes and the calculations based on the Mie theory is also shown in Figure 7 for all four spectral bands. Lines that indicate no nonsphericity (solid line) and varying degrees of nonsphericity effect (dashed line = 30% and dotted line = 50%) are plotted. The uncertainty in the dust particle size and the measurements variability is shown by the error bars. Most of the points for $\lambda > 0.6$ μm

Table 4c. Slopes $\Delta\rho^*/\Delta\tau$ at Scattering Angle of 120° and 90°

	$\Theta = 120°$				$\Theta = 90°$			
	0.44 μm	0.67 μm	0.87 μm	1.02 μm	0.44 μm	0.67 μm	0.87 μm	1.02 μm
Banizoumbou 1996	0.050	0.111	0.121	0.120	0.078	0.144	0.148	0.145
Banizoumbou 1997	0.030	0.112	0.111	0.120	0.054	0.141	0.146	0.151
Sal Island 1994–1995	0.028	0.110	0.100	0.103	0.020	0.141	0.141	0.146
Sal Island 1996–1997	0.019	0.089	0.082	0.080	0.054	0.126	0.120	0.113
Sede Boker 1996–Jan./June	0.038	0.123	0.130	0.120	0.067	0.154	0.161	0.149
Sede Boker 1998–May/Oct.	0.033	0.156	0.168	0.167	0.073	0.186	0.198	0.195
Theoretical computation $\rho_s = 0.0$; $R_{\text{eff}} = 1.5$ μm	0.054	0.093	0.103	0.108	0.079	0.128	0.140	0.146
Theoretical computation $\rho_s = 0.0$; $R_{\text{eff}} = 2.5$ μm	0.059	0.116	0.158	0.166	0.089	0.151	0.195	0.203
Theoretical computation $\rho_s = 0.1; 0.2; 0.4; 0.4/$; $R_{\text{eff}} = 1.5$ μm	0.047	0.078	0.090	0.098	0.071	0.113	0.127	0.136
Theoretical computation $\rho_s = 0.1; 0.2; 0.4; 0.4/$; $R_{\text{eff}} = 2.5$ μm	0.052	0.100	0.143	0.153	0.081	0.135	0.180	0.191

Theoretical computations are given for two aerosol models ($R_{\text{eff}} = 1.5$ and 2.5 μm) using the Mie theory, first with a black surface, then over a reflecting surface with an albedo of 0.1, 0.2, 0.4, and 0.4 at 0.44 μm, 0.67 μm, 0.87 μm, and 1.02 μm.

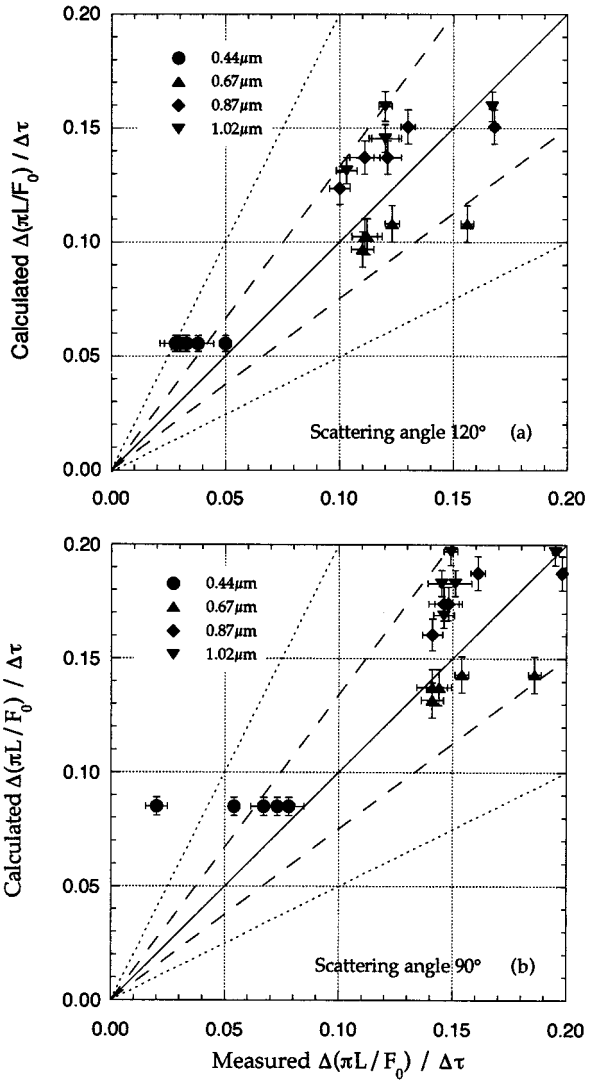

Figure 7. Scatterplots of the slopes $\Delta(\Pi L/F_0)/\Delta\tau$, between the calculated values using Mie theory and the values derived from the AERONET measurements for the four spectral bands of the AERONET instruments. Results are given for scattering angles of (a) 120° and (b) 90°. The calculated values are for the average between the two dust effective radius of 1.5 and 2.5 μm. The error bars show the variation due to this uncertainty. The measured error bars are the standard deviation of the slopes. Solid line indicates no nonsphericity effect, the dashed line, a 30% degree of nonsphericity effect, and the dotted line, a 50% degree of nonsphericity effect.

are within 15–30% of the spherical value. This may indicate a slight nonsphericity effect but not so strong as expected from theoretical computations for prolate or oblate spheroids with large aspect ratios [*Mishchenko et al*., 1997]. Based on the present accuracy, the aspect ratio is not larger than 1.2–1.4 [*Mishchenko et al*., 1997]. Measurements in larger scattering angles, 150° and upper, which are difficult to get from ground, are needed for making a definitive statement. The values for 0.44 μm are more variable and dominated by the presence of absorption that is not included in the calculations of Figure 7.

Let us recall that the present analysis is limited to optical thickness smaller than 0.6 and that strong dust events, with larger particles that are expected to be nonspherical, are not considered.

4.6. Possible Interaction of Particle Nonsphericity and Single-Scattering Albedo Effects

Some particle shapes can, in principle, introduce nonspherical effects for scattering angles around 148° [*Mishchenko et al*., 1997]. An error in the path radiance, due to the assumption of spherical particles, can introduce an uncertainty in the derivation of the single-scattering albedo. Fortunately, the sensitivity of the satellite radiance to aerosol absorption over the land and the ocean is different, and therefore requirements of consistency over land and ocean can be used to narrow the uncertainty introduced from possible nonsphericity effects. Note that the Landsat data over the land and ocean were taken within 10 km of each other, thus we expect to have the same dust optical properties and optical thickness.

In Tables 5a and 5b, results of quantitative tests are shown for the effect of nonsphericity on the consistency of the apparent reflectance over the land and the ocean for a wavelength of 0.865 μm. We assume that nonsphericity effects impact the phase function and result in errors in path radiance. For a given value of the effective radius (1.5 μm in Table 5a and 2.5 μm in Table 5b) we select several values of the imaginary index n_ι (column 1) and adjust the value of the path radiance so that the change in the brightness between the clear and the dusty days will remain roughly equal to the Landsat values measured over the ocean (columns 3 and 4). The ratio L_{NS}/L_S between the path radiance for spherical and nonspherical assumption can be derived (column 5). Then, using the same aerosol properties, we derive the radiances over the land for the hazy day (column 7), the clear day (column 6) being used to derived the surface contribution. It is clear that there is a larger and larger discrepancy as the absorption increases and that the nonsphericity effect derived over the ocean is not able to compensate for. The ratio L_{NS}/L_S between the path radiances for spherical and nonspherical assumption for the hazy day that would be required is reported in column 8.

The two ratios have been plotted as a function of the imaginary part of the refractive index in Figure 8. Consistency requires that for a same effective radius the two solid lines (or dashed lines) in Figure 8 cross each other, resulting in the same nonsphericity and absorption over the land and ocean, which happens near an imaginary index of zero. Larger nonsphericity, compensated by higher absorption over the ocean, produces even stronger inconsistencies over the land. The conclusion is that the data do not support nonsphericity effect of more than around 20% at the scattering angle of 148°, with corresponding error in the single-scattering albedo of ± 0.01. The overall error in the derived single-scattering albedo is in the range of $\Delta\omega_0 = \pm 0.01$ to ± 0.02. Again, strong nonsphericity effects could be detected at larger scattering angles, but they are not reachable from Landsat TM.

5. Discussion, Comparison With Literature

The knowledge of the dust properties in the literature is very scattered. The information is based on in situ measurements taken on ground level and may not represent the whole vertical column. The efficiency of dust sampling used in these measurements may depend on the particle size [*Fouquart et al*., 1987a]. The properties of the dust aerosol may also vary due to variability of sources, or distance from the source [*Sokolik et*

Table 5a. Sensitivity of the Apparent Reflectance at 0.865 μm Over the Land and Ocean to the Dust Absorption and Nonsphericity Effect, Effective Radius of 1.5 μm

	TM Reflectance			TM Reflectance		
	Ocean, Clear	Ocean, Hazy		Land, Clear	Land, Hazy	
1.5 μm	0.09	0.23		0.300	0.374	
	Reflectance		Ratio	Reflectance		Ratio
n_i ω_0	Ocean, Clear	Ocean, Hazy	L_{NS}/L_S	Land, Clear	Land, Hazy	L_{NS}/L_S
0.000 1.00	0.09	0.23	0.91	0.301	0.378	0.92
0.001 0.98	0.09	0.23	1.04	0.298	0.361	1.12
0.002 0.96	0.09	0.23	1.18	0.300	0.353	1.32
0.002 0.93	0.09	0.23	1.42	0.295	0.332	1.73

For each effective radius and imaginary index n_i the degree of the nonspherical effect on the phase function was adjusted so that the reflectance will equal the TM-measured reflectance both for the hazy and the clear days. The resultant ratio of the nonspherical radiance to the spherical radiance is given by L_{NS}/L_S. Since the dust nonsphericity did not change across the short distance from land to ocean, consistency requires that the value of L_{NS}/L_S over land and ocean should be the same. It is achieved at $n_i \sim 0.000$ and $L_{NS}/L_S \sim 1.0$.

al., 1998] although *Carlson and Benjamin* [1980] pointed that measurements during the GATE experiments show that successive outbreaks of dust closely resemble each other in the chemical composition and particle size.

The particle effective radius varies between 1.2 μm and 20 μm modes for the dust storm model of *Shettle* [1984] and 0.5 μm in the radiative forcing calculations of *Tegen et al*. [1996]. Measurements of *Levin et al*. [1980] for dust storms over the Israeli desert and *Patterson and Gillette* [1977] over Texas also show that the dust surface area distribution has a maximum around 2 μm. Dust originating from China was measured over Japan also to have particle size around 2 μm [*Tanaka et al*., 1989].

The spectral imaginary index and single-scattering albedo indicate that dust has significantly less absorption than in the *WMO* [1983] and AFGL (Air Force Geophysical Laboratory) models [*Jursa*, 1985], down to zero in the central part of the solar spectrum. In the literature we notice a divergence between dust absorption reported from in situ measurements and absorption inferred from the radiation field in the atmosphere. In situ measurements indicate the presence of dust absorption in the visible part of the spectrum, summarized as $n_i = -0.008$ by the WMO and AFGL models. Some lower absorption was indicated by *Levin et al*. [1980] of $n_i = -0.003$ for heavy dust in the center of the visible. While in the blue and UV parts of the spectrum the absorption can be due to iron compounds [*Sokolik and Toon*, 1997; *Claquin et al*., 1999], the reason for the absorption in the visible is not clear and was suggested to originate from the presence of black carbon that accompanies the dust [*Lindberg*, 1975]. *Levin et al*. [1980] noticed a reduction of the dust absorption with increase of the optical thickness in the dust storm events, due to the smaller impact of urban aerosol component. The model of *Carlson and Benjamin* [1980], used to calculate dust heating, did have absorption that is lower than the WMO model. Optical measurements of the aerosol absorption, derived from flux or radiance measurements do not indicate the presence of measurable absorption. Flux divergence measured from aircraft by *Fouquart et al*. [1987b] for the broad solar spectrum indicate very small absorption, with $\omega_0 = 0.95$, comparable to the present finding. *Otterman et al*. [1982] derived an imaginary index of $n_i = -0.001 \pm 0.001$ from Landsat images for $\lambda = 0.55$ to 1 μm over the Persian Gulf region, also indicating the possibility that dust is not absorbing. Interesting is the finding of *Ackerman and Chung* [1992] that derived single-scattering albedo of dust from aircraft measurements of 0.73–0.80 in the

Table 5b. Sensitivity of the Apparent Reflectance at 0.865 μm Over the Land and Ocean to the Dust Absorption and Nonsphericity Effect, Effective Radius of 2.5 μm

	TM Reflectance			TM Reflectance		
	Ocean, Clear	Ocean, Hazy		Land, Clear	Land, Hazy	
2.5 μm	0.09	0.23		0.300	0.374	
	Reflectance		Ratio	Reflectance		Ratio
n_i ω_0	Ocean, Clear	Ocean, Hazy	L_{NS}/L_S	Land, Clear	Land, Hazy	L_{NS}/L_S
0.000 1.00	0.09	0.23	0.97	0.298	0.381	0.94
0.001 0.97	0.09	0.23	1.20	0.299	0.359	1.30
0.002 0.94	0.09	0.23	1.42	0.300	0.346	1.66
0.002 0.90	0.09	0.23	1.84	0.297	0.322	2.37

For each effective radius and imaginary index n_i the degree of the nonspherical effect on the phase function was adjusted so that the reflectance will equal the TM-measured reflectance both for the hazy and the clear days. The resultant ratio of the nonspherical radiance to the spherical radiance is given by L_{NS}/L_S. Since the dust nonsphericity did not change across the short distance from land to ocean, consistency requires that the value of L_{NS}/L_S over land and ocean should be the same. It is achieved at $n_i \sim 0.000$ and $L_{NS}/L_S \sim 1.0$.

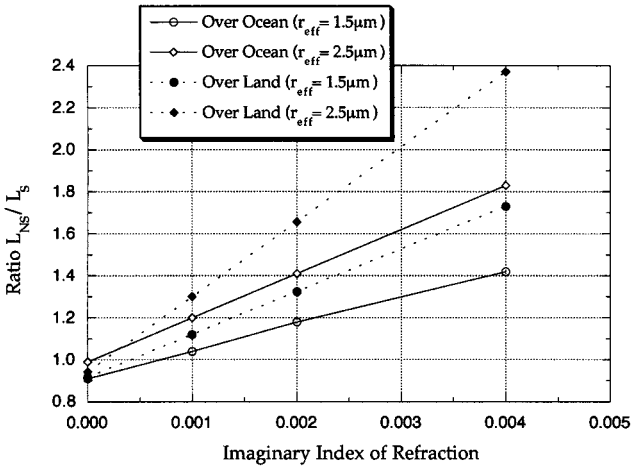

Figure 8. Value of nonsphericity, defined as the ratio of the nonspherical path radiance to the spherical path radiance, required to compensate for dust absorption (by means of the imaginary part of the refractive index). Results are given at 0.865 μm for an assumed particles radius of 1.5 μm (circles) and 2.5 μm (diamonds).

visible channels, but found that using these values in a radiative transfer model does not fit the ERBE measurements of the effects of dust on the reflected solar flux to space over the bright desert. While the model predicts a reduction of the flux by 20–60 W/m^2 due to absorption, ERBE data do not show any considerable change. The only exception is a high imaginary index of 0.01 used by *Moulin et al*. [1997], but it was used to fit the high value of the phase function required to explain satellite-measured radiance, rather than absorption and probably corresponds to uncertainty in the size distribution or the enhancement of side scattering by the particle nonsphericity.

Nonsphericity, derived from the present measurements is in the same range of the results of *Kaufman et al*. [1994] and lower than the nonsphericity measured by *Nakajima et al*. [1989] for yellow dust over Japan. It is possible that long-range transport of dust removes the very large particles and covers others by hydroscopic compounds, reducing the nonsphericity effect. It is also possible that nonsphericity effects are not detected because of the range of scattering angles which do not include the backscattered directions [*Yang et al*., 2000].

6. Conclusion

A novel approach is described to derive a detailed characterization of the optical properties of aerosol using a combination of spectral remote sensing from ground-based radiometers and space-borne spectral measurements taken across the solar spectrum over land and ocean. The technique is applied to Saharan desert dust deriving a climatology of the undisturbed dust optical properties, of direct relevance for climate modeling. The desert aerosol size distribution was derived from the aureole measurements in three locations around the Sahara desert. In addition to the coarse particles at a radius of 1–5 μm, a mode around 0.5 μm radius was found, for desert aerosols in sites that are strongly influenced by dust.

For wavelengths larger than 0.55 μm, dust was found to be less absorbing than previous measurements predicted. Even in the blue, we did not find values of single-scattering albedo less than 0.8, as reported in the literature. The real part of the refractive index was found to be much less dependent on the wavelength and does not reach 1.22 at 2.1 μm, a more realistic value of 1.46 has to be considered.

Finally, the evaluation of the dust optical properties due to nonsphericity, for scattering angles up to 120°, shows that the effect on the radiances is not significant. Mie theory was able to predict the dust effect on the radiance with errors smaller than 30% (for optical thickness smaller than 0.6). Even these errors were not consistent with models of the effect of nonsphericity. For scattering angles around 180°, of interest to lidar returns, nonsphericity is probably still very important.

Acknowledgments. The AERONET Sun photometer/radiometer data were processed by I. Slutsker and the TM data by S. Mattoo. We wish to express our gratitude to M. Santos Soares, Director of the Servico National de Meteorologia e Geophysica (SNMG), Cape Verde, to A. Werem from the Institut d'Energie Solaire, Burkina Faso, to O. Manga from the University of Niamey, Niger, and to J. L. Rajot from ORSTOM/IRD, France, for their help in maintaining the AERONET instruments.

References

Ackerman, S. A., and H. Chung, Radiative effects of airborne dust on regional energy budgets at the top of the atmosphere, *J. Appl. Meteorol*., *31*, 223–233, 1992.

Ahmad, Z., and R. S. Fraser, An iterative radiative transfer code for ocean-atmosphere system, *J. Atmos. Sci*., *39*, 656–665, 1982.

Bergametti, G., L. Gomes, E. Remoudaki, M. Desbois, D. Martin, and P. Buat-Ménard, Present transport and deposition patterns of African dusts to the northwestern Mediterranean, in *Paleoclimatology and Paleometeorology: Modern and Past Patterns of Global Atmospheric Transport*, edited by M. Leinen and M. Sarnthein, pp. 227–252, Kluwer Acad., Norwell, Mass., 1989.

Braaten, D. A., and T. A. Cahill, Size and composition of Asian dust transported to Hawaii, *Atmos. Environ*., *20*, 1105–1109, 1986.

Carlson, T. N., Atmospheric turbidity in Saharan dust outbreaks as determined by analyses of satellite brightness data, *Mon. Weather Rev*., *107*, 322–335, 1979.

Carlson, T. N., and S. G., Benjamin, Radiative heating rates of Saharan dust, *J. Atmos. Sci*., *37*, 193–213, 1980.

Chester, R., E. J. Sharples, G. S. Sanders, and A. C. Saydam, Saharan dust incursion over the Tyrrhenian Sea, *Atmos. Environ*., *18*, 929–935, 1984.

Chiapello, I., J. M. Prospero, J. R. Herman, and N. C. Hsu, Detection of mineral dust over the North Atlantic Ocean and Africa, *J. Geophys. Res*., *104*, 9277–9291, 1999.

Claquin T., M. Schulz, and Y. J. Balkanski, Modeling the mineralogy of atmospheric dust source, *J. Geophys. Res*., *104*, 22,243–22,256, 1999.

d'Almeida, G. A., P. Koepke, and E. P. Shettle, *Atmospheric Aerosols, Global Climatology and Radiative Characteristics*, A. Deepak, Hampton, Va., 1991.

Dubovik, O., B. N. Holben, Y. J. Kaufman, M. Yamasoe, A. Smirnov, D. Tanré, and I. Slutsker, Single-scattering albedo of smoke retrieved from the sky radiance and solar transmittance measured from the ground, *J. Geophys. Res*., *103*, 31,903–31,924, 1998.

Dubovik, O., A. Smirnov, B. N. Holben, M. D. King, Y. J. Kaufman, T. F. Eck, and I. Slutsker, Accuracy assessments of aerosol properties retrieved from Aerosol Robotic Network (AERONET) Sun and sky measurements, *J. Geophys. Res*., *105*, 9791–9806, 2000.

Duce, R. A., C. K. Unni, B. J. Ray, J. M. Prospero, and J. T. Merrill, Long-range atmospheric transport of soil dust from Asia to the tropical North Pacific: Temporal variability, *Science*, *209*, 1522–1524, 1980.

Dulac, F., D. Tanré, G. Bergametti, P. Buat-Menard, M. Desbois, and D. Sutton, Assessment of the African airborne dust mass over the western Mediterranean Sea using Meteosat data, *J. Geophys. Res*., *97*, 2489–2506, 1992.

Ferrare, R. A., R. S. Fraser, and Y. J. Kaufman, Satellite remote sensing of large-scale air pollution—Measurements of forest fires smoke, *J. Geophys. Res*., *95*, 9911–9925, 1990.

Fouquart, Y., B. Bonnel, M. C. Roquai, R. Santer, and A. Cerf,

Observations of Saharan aerosols: Results of ECLATS field experiment, I, Optical thickness and aerosol size distribution, *J. Clim. Appl. Meteorol*., *26*, 28–37, 1987a.

Fouquart, Y., B. Bonnel, J. C. Brogniez, L. Buriez, L. Smith, and J. J. Morcrette, Observations of Saharan aerosols: Results of ECLATS Field experiment, II, Broadband radiative characteristics of the aerosols and vertical radiative flux divergence, *J. Clim. Appl. Meteorol*., *25*, 38–52, 1987b.

Fraser, R. S., and Y. J. Kaufman, The relative importance of aerosol scattering and absorption in remote sensing, *IEEE J. Geosci. Remote Sens*., *GE-23*, 525–633, 1985.

Glaccum, R. A., and J. M. Prospero, Saharan aerosols over the tropical North Atlantic: Mineralogy, *Mar. Geol*., *37*, 295–321, 1980.

Heintzenberg, J., R. J. Charlson, A. D. Clarke, C. Liousse, V. Ramaswany, K. P. Shine, M. Wendish, and G. Helas, Measurements and modelling of aerosol single-scattering albedo: Progress, problems and prospects, *Beitr. Phys. Atmos*., *70*, 249–263, 1997.

Herman, J. R., P. K. Barthia, O. Torres, C. Hsu, C. Seftor, and E. Celarier, Global distribution of UV absorbing aerosol from Nimbus 7/TOMS data, *J. Geophys. Res*., *102*, 16,911–16,922, 1997.

Holben, B. N., et al., AERONET-A federated instrument network and data archive for aerosol characterization, *Remote Sens. Environ*., *66*, 1–16, 1998a.

Holben, B. N., et al., Aerosol climatology measured from the globally distributed ground-based AERONET system, paper presented at the Joint International Symposium on Global Atmospheric Chemistry, IGAC, Seattle, Washington, 1998b.

Husar, R. B., J. Prospero, and L. L. Stowe, Characterization of tropospheric aerosols over the oceans with the NOAA-AVHRR aerosol optical thickness operational product, *J. Geophys. Res*., *102*, 16,889–16,909, 1997.

Jaenicke, R., and L. Schütz, Comprehensive study of physical and chemical properties of the surface aerosols in the Cape Verde Islands region, *J. Geophys. Res*., *83*, 3585–3599, 1978.

Joseph, J. H., The sensitivity of a numerical model of the global atmosphere to the presence of desert aerosol, in *Aerosols and Their Climatic Effects*, edited by H. E. Gerber and A. Deepak, pp. 215–226, A. Deepak, Hampton, Va., 1984.

Jursa, A. S. (Ed.), *Handbook of Geophysics*, Air Force Geophys. Lab., Springfield, Va., 1985.

Kaufman, Y. J., Satellite sensing of aerosol absorption, *J. Geophys. Res*., *92*, 4307–4317, 1987.

Kaufman, Y. J., R. S. Fraser, and R. A. Ferrare, Satellite remote sensing of large-scale air pollution—Method, *J. Geophys. Res*., *95*, 9895–9909, 1990.

Kaufman, Y. J., A. Gitelson, A. Karnieli, E. Ganor, R. S. Fraser, T. Nakajima, S. Mattoo, and B. N. Holben, Size distribution and phase function of aerosol particles retrieved from sky brightness measurements, *J. Geophys. Res*., *99*, 10,341–10,356, 1994.

Levin, Z., J. H. Joseph, and Y. Mekler, Properties of Sharav (Khamsin) dust—Comparison of optical and direct sampling data, *J. Atmos. Sci*., *37*, 882–891, 1980.

Li, X., H. Maring, D. Savoie, K. Voss, and J. M. Prospero, Dominance of mineral dust in aerosol light scattering in the North Atlantic trade winds, *Nature*, *380*, 416–419, 1996.

Lindberg, J. D., The composition and optical absorption coefficient of atmospheric particulate matter, *Opt. Quant. Electron*., *7*, 131–139, 1975.

Mishchenko, M. I., L. D. Travis, R. A. Kahn, and R. A. West, Modeling phase functions for dustlike tropospheric aerosols using a shape mixture of randomly oriented polydisperse spheroids, *J. Geophys. Res*., *102*, 16,831–16,847, 1997.

Morales, C., The airborne transport of Saharan dust: A review, *Clim. Change*, *9*, 219–241, 1986.

Moulin, C., F. Dulac, C. E. Lambert, P. Chazette, I. Jankowiak, B. Chatenet, and F. Lavenu, Long-term daily monitoring of Saharan dust load over ocean using Meteosat ISCCP-B2 data, 2, Accuracy of the method and validation using Sun photometer measurements, *J. Geophys. Res*., *102*, 16,959–16,970, 1997.

Nakajima, T., M. Tanaka, M. Yamano, M. Shiobara, K. Arao, and Y. Nakanishi, Aerosol optical characteristics in the yellow sand events observed in May, 1982 at Nagasaki, part 2, Models, *J. Meteorol. Soc. Jpn*., *67*, 279–291, 1989.

Nakajima, T., G. Tonna, R. Rao, P. Boi, Y. Kaufman, and B. Holben, Use of sky brightness measurements from ground for remote sensing of particulate polydispersions, *Appl. Opt*., *35*, 2672–2686, 1996.

Otterman, J., R. S. Fraser, and O. P. Bahethi, Characterization of tropospheric desert aerosols at solar wavelengths by multispectral radiometry from Landsat, *J. Geophys. Res*., *87*, 1270–1278, 1982.

Patterson, E. M., and D. A. Gillette, Commonalities in measured size distribution for aerosol having a soil-derived component, *J. Geophys. Res*., *82*, 2074–2082, 1977.

Prospero, J. M., Eolian transport to the world ocean, The sea, vol. 7, in *The Oceanic Lithosphere*, edited by C. Emiliani, pp. 801–874, John Wiley, New York, 1981.

Prospero, J. M., M. Uematsu, and D. L. Savoie, Mineral aerosol transport to the Pacific Ocean, in *Chemical Oceanography*, vol. 10, edited by J. P. Riley, R. Chester, and R. A. Duce, pp. 188–218, Academic, San Diego, Calif., 1989.

Pye, K., *Aeolian Dust and Dust Deposit*, 335 pp., Academic, San Diego, Calif., 1987.

Reiff, J., G. S. Forbes, F. T. M. Spieksma, and J. J. Reynders, African dust reaching northwestern Europe: A case study to verify trajectory calculations, *J. Clim. Appl. Meteorol*., *25*, 1543–1567, 1986.

Remer, L. A., and Y. J. Kaufman, Dynamical aerosol model: Urban/industrial aerosol, *J. Geophys. Res*., *103*, 13,859–13,871, 1998.

Remer, L. A., Y. J. Kaufman, B. N. Holben, A. M. Thompson, and D. McNamara, Biomass burning aerosol size distribution and modeled optical properties, *J. Geophys. Res*., *103*, 31,879–31,891, 1998.

Remer, L. A., Y. J. Kaufman, and B. N. Holben, Interannual variation of ambient aerosol characteristics on the east cost of the United States, *J. Geophys. Res*., *104*, 2223–2231, 1999.

Santer, R., and M. Herman, Particle size distribution from forward scattered light using the Chahine inversion scheme, *Appl. Opt*., *22*, 2294–2302, 1983.

Schütz, L., Sahara dust transport over the North Atlantic ocean—Model calculations and measurements, in *Saharan Dust*, edited by C. Morales, pp. 267–277, John Wiley, New York, 1979.

Shaw, G. E., Transport of Asian desert aerosol to the Hawaiian Islands, *J. Appl. Meteorol*., *19*, 1254–1259, 1980.

Shettle, E. P., Optical and radiative properties of a desert aerosol model, in *Proceedings of the Symposium on Radiation in the Atmosphere*, edited by G. Fiocco, pp. 74–77, A. Deepak, Hampton, Va., 1984.

Sokolik, I. N., and O. B. Toon, Direct radiative forcing by anthropogenic airborne mineral aerosol, *Nature*, *381*, 681–683, 1996.

Sokolik, I. N., O. B. Toon, and R. W. Bergstrom, Modeling of the radiative characteristics of airborne mineral aerosol at IR wavelengths, *J. Geophys. Res*., *103*, 8813–8826, 1998.

Talbot, R. W., R. C. Harris, E. V. Browell, G. L. Gregory, D. I. Sebacher, and S. M. Beck, Distribution and geochemistry of aerosols in the tropical North Atlantic troposphere: Relationship to Saharan dust, *J. Geophys. Res*., *91*, 5173–5182, 1986.

Tanaka, M., T. Nakajima, M. Shiobara, M. Yamano, and K. Arao, Aerosol optical characteristics in the yellow sand events observed in May, 1982 at Nagasaki, part 1, Observations, *J. Meteorol. Soc. Jpn*., *67*, 267–278, 1989.

Tanré, D., J. F. Geleyn, and J. Slingo, First results of the introduction of an advanced aerosol-radiation interaction in the ECMWF low resolution global model, in *Aerosols and Their Climatic Effects*, edited by H. E. Gerber and A. Deepak, pp. 133–177, A. Deepak, Hampton, Va., 1984.

Tanré, D., P. Y. Deschamps, C. Devaux, and M. Herman, Estimation of Saharan aerosol optical thickness from blurring effects in Thematic Mapper data, *J. Geophys. Res*., *93*, 15,955–15,964, 1988a.

Tanré, D., C. Devaux, M. Herman, R. Santer, and J. Y. Gac, Radiative properties of desert aerosols by optical ground-based measurements at solar wavelengths, *J. Geophys. Res*., *93*, 14,223–14,231, 1988b.

Tegen, I., A. A. Lacis, and I. Fung, The influence on climate forcing of mineral aerosols from disturbed soils, *Nature*, *380*, 419–422, 1996.

Von Hoyningen-Huene, W., and P. Posse, Nonsphericity of aerosol particles and their contribution to radiative forcing, *J. Quant. Spectrosc. Radiat. Transfer*, *57*, 651–668, 1997.

Wendish, M., and W. Von Hoyningen-Huene, Possibility of refractive index determination of atmospheric aerosol particles by ground-based solar extinction and scattering measurements, *Atmos. Environ*., *28*, 785–792, 1994.

World Meteorological Organization (WMO), Radiation commission of IAMAP meeting of experts on aerosol and their climatic effects, *WCP55*, Geneva, Switzerland, 1983.

Yang, P., K. N. Liou, M. I. Mishchenko, and B.-C. Gao, Efficient finite-difference time-domain scheme for light scattering by dielec-

tric particles: Application to aerosols, *Appl. Opt*., *39*, 3727–3737, 2000.

L. Blarel and D. Tanré, Laboratoire d'Optique Atmosphérique, CNRS, Université des Sciences et Technologies de Lille, 59655 - Villeneuve d'Ascq, France. (tanre@loa.univ-lille1.fr)

B. Chatenet, Laboratoire Interuniversitaire des Systèmes Atmosphériques, CNRS, Universités Paris VII et Paris XII, 94010-Créteil Cedex, France.

O. Dubovik and A. Smirnov, Science Systems and Applications Inc., Laboratory for Terrestrial Physics, NASA GSFC, Greenbelt, MD 20771.

B. N. Holben, NASA GSFC, Laboratory for Terrestrial Physics, Greenbelt, MD 20771.

A. Karnieli, Institute for Desert Research, Ben Gurion University, Sede-Boker, Israel.

Y. J. Kaufman and L. A. Remer, NASA GSFC, Laboratory for Atmospheres, Greenbelt, MD 20771.

F. Lavenu, CESBIO CNES, 18, Avenue Ed. Belin, 31401-Toulouse Cedex, France.

(Received January 27, 2000; revised September 18, 2000; accepted September 20, 2000.)